Theor. Comput. Fluid Dyn.
DOI 10.1007/s00162-017-0432-2

ORIGINAL ARTICLE

Maziar S. Hemati · Clarence W. Rowley · Eric A. Deem · Louis N. Cattafesta

De-biasing the dynamic mode decomposition for applied Koopman spectral analysis of noisy datasets

Received: 17 October 2015 / Accepted: 5 April 2017

Abstract The dynamic mode decomposition (DMD)—a popular method for performing data-driven Koopman spectral analysis—has gained increased popularity for extracting dynamically meaningful spatiotemporal descriptions of fluid flows from snapshot measurements. Often times, DMD descriptions can be used for predictive purposes as well, which enables informed decision-making based on DMD model forecasts. Despite its widespread use and utility, DMD can fail to yield accurate dynamical descriptions when the measured snapshot data are imprecise due to, e.g., sensor noise. Here, we express DMD as a two-stage algorithm in order to isolate a source of systematic error. We show that DMD's first stage, a subspace projection step, systematically introduces bias errors by processing snapshots asymmetrically. To remove this systematic error, we propose utilizing an augmented snapshot matrix in a subspace projection step, as in problems of total least-squares, in order to account for the error present in all snapshots. The resulting unbiased and noise-aware total DMD (TDMD) formulation reduces to standard DMD in the absence of snapshot errors, while the two-stage perspective generalizes the de-biasing framework to other related methods as well. TDMD's performance is demonstrated in numerical and experimental fluids examples. In particular, in the analysis of time-resolved particle image velocimetry data for a separated flow, TDMD outperforms standard DMD by providing dynamical interpretations that are consistent with alternative analysis techniques. Further, TDMD extracts modes that reveal detailed spatial structures missed by standard DMD.

Keywords Data-driven dynamical systems · Koopman spectral analysis · Total least-squares · Sensor noise · Reduced-order model · Experimental fluid mechanics

This work was supported by the Air Force Office of Scientific Research under Grant FA9550-14-1-0289 and the Office of Naval Research under MURI Grant 00014-14-1-0533. M.S.H. gratefully acknowledges support from the Department of Aerospace Engineering and Mechanics at the University of Minnesota.

Communicated by Oleg V. Vasilyev.

Electronic supplementary material The online version of this article (doi:10.1007/s00162-017-0432-2) contains supplementary material, which is available to authorized users.

M. S. Hemati (✉)
Aerospace Engineering and Mechanics, University of Minnesota, Minneapolis, MN 55455, USA
E-mail: mhemati@umn.edu
Tel.: +612-625-6857

C. W. Rowley
Mechanical and Aerospace Engineering, Princeton University, Princeton, NJ 08544, USA

E. A. Deem · L. N. Cattafesta
Florida Center for Advanced Aero-Propulsion, Florida State University, Tallahassee, FL 32310, USA

Published online: 17 April 2017

1 Introduction

Dynamical systems—mathematical representations of a system's time evolution—are of great importance and utility in the natural, social, and applied sciences, as they can provide a means of describing—and, therefore, better understanding—complex phenomena. Often times, dynamical models can also be used in a predictive manner, to forecast the future behavior of a particular system, from which actionable decisions can be made. Still, reliable and insightful models can be difficult to formulate in the context of nonlinear systems, such as fluid flows, which can exhibit complex behaviors on a broad range of spatial and temporal scales. For instance, while fluid flows can be described mathematically from first-principles physics-based modeling (e.g., the Navier–Stokes equations), such models often lack closed-form solutions; although numerical solutions can be sought, significant computational resources may be required, which can make analysis and prediction unwieldy and impractical. Even in instances for which a numerical solution can be reasonably computed, the resulting data—on their own—will not necessarily provide useful insight into the underlying characteristics of the fluid flow evolution. Furthermore, for many dynamical systems, first-principles modeling can be prohibitively challenging due to the sheer scale and complexity of the system dynamics; in such instances, the best recourse may be to determine a model from empirical data collected through system observations (i.e., a *data-driven* approach).

In an effort to address these modeling challenges, the dynamic mode decomposition (DMD) was developed in the fluid mechanics community as an equation-free data-driven technique capable of extracting dynamically relevant spatial structures and associated temporal characteristics (i.e., growth/decay rates and oscillation frequencies) from snapshot observations (e.g., pressure, velocity, vorticity) sampled from a fluid flow [43,46]. It was shown in [42] that DMD approximates the *Koopman operator* [31], an infinite-dimensional *linear* operator that describes the evolution of a *nonlinear* dynamical system by its action on observables (defined precisely in the next section). One may then study the dynamics of a nonlinear system using the spectral properties of this linear operator [32]: For instance, von Neumann used this perspective in his celebrated proof of the mean ergodic theorem [53]. Owing to its applicability in modeling nonlinear systems and to its demonstrated success in analyzing complex fluid flows, DMD has gained increasing popularity in fluid mechanics and beyond. For instance, DMD has been utilized in the fields of epidemiology [41], medicine [5], neuroscience [7], power systems [8], robotics [4], sustainable buildings [8], and video processing [22].

Part of DMD's growth in popularity can be attributed to its potential for use as a model reduction technique. The dynamics of fluid flows, like many large-scale systems, can often be represented in a low-dimensional manner, provided an appropriate coordinate system is utilized. For example, the low-dimensional nature of fluid flow evolution has been well established in the context of the laminar flow over a cylinder in two spatial dimensions [40]. Numerous such models have been constructed using the proper orthogonal decomposition (POD)—a modal decomposition technique that extracts coherent structures from snapshot data [28]; however, POD-based approaches require additional modeling considerations to yield low-dimensional *dynamic* representations of fluid flows. In contrast, DMD extracts *both* a set of coherent spatial structures *and* their associated (simple) dynamics, making it appealing from a dynamic modeling perspective: Modes can be categorized as "slow" or "fast" based on their relative growth/decay rates, as in Davison's method [10], providing a rationale for neglecting certain modal responses for the purpose of model reduction.

With the aim of constructing low-dimensional representations of complex large-scale dynamics, various methods for rank-reduction and optimal mode selection have been developed around DMD [9,21,29,58]. Furthermore, as a modeling technique, DMD has connections to common "data-driven" methods from system identification (e.g., Ho's Algorithm [27], Kung's Algorithm [33], and the eigensystem realization algorithm (ERA) [30]), atmospheric science (e.g., linear inverse modeling (LIM) and principal interaction/oscillation pattern analysis [25]), signal processing (e.g., Prony's Method [34]), and time series analysis (e.g., autoregressive models [6]). A detailed discussion of DMD's connections with ERA and LIM is presented in [50]. Finally, we note that while DMD can be used in a model reduction capacity, it is also a versatile method for data exploration—much in the way that POD has been used for such purposes; insights can be gleaned by analyzing the spatially coherent structures along with their associated temporal characteristics, bringing to light the "active regions" of a flow in terms of their contributions to the overall flow dynamics. For instance, DMD has allowed experimental data to be analyzed to gain a better understanding for the instability mechanisms associated with aerodynamically driven annular liquid sheets [12].

Despite increasing adoption as a modeling and analysis tool, the adverse influence of measurement errors on DMD's performance and reliability remains under-appreciated. For instance, the signal-to-noise ratio of the observed snapshot data can alter the growth/decay rates predicted by DMD [13]—an obvious problem

for studies that rely upon DMD to identify and distinguish between stable and unstable spatial modes. Even when questions of stability are not a concern, the sensitivity of growth/decay rates to measurement noise can potentially lead to a misinterpretation of the role of particular modes and their contribution to the dynamics; incorrect approximations of the damping of dynamic modes will alter the discrimination of "slow" and "fast" modes, thus misguiding a model reduction approach grounded in timescale arguments. Numerous other studies have also encountered DMD's sensitivity to measurement errors (e.g., sensor noise), which has led to a host of approaches aimed at mitigating noise-related effects via various forms of rank-reduction, ensemble averaging, cross-validation, and windowing [12,26,43–45,47,50,58]. As we will show, although these techniques provide a means of uniquely determining a DMD realization, the resulting analysis will be subject to systematic bias errors when the measured snapshot data are inexact due to sensor noise or other effects. By viewing DMD as a "best-fit" least-squares/minimum-norm operator determined from measured snapshot data, we establish that the same sources of noise-induced bias arising in standard least-squares problems—extensively studied in statistics and numerical analysis [14–16,19,20,35,52,59]—will also plague DMD.

In this manuscript, we address the issue of noise-induced bias by focusing on the DMD algorithm directly. We show that the currently used formulation of DMD accounts for errors in only some of the snapshots, whereas measurement noise typically influences *all* snapshots. Invariably, accounting for noise in only a subset of the data will lead to biases, since doing so amounts to treating the remaining data as exact. To arrive at an unbiased result, we propose a *total least-squares/error-in-variables* formulation of DMD, such that errors in *all* the data are considered. Here, we focus on de-biasing DMD from an algorithmic standpoint; an analytical characterization of the influence of sensor noise on DMD and alternative de-biasing strategies are considered in the complementary work by Dawson et al. [11]. In particular, we introduce a de-biasing framework that can be generalized to other DMD-like algorithms. To arrive at such a framework, we focus on simplifying the unbiased formulation of DMD in a manner that decouples the de-biasing aspects of the framework from the particular choice of DMD-like algorithm—a feature that can be realized from a projection operator perspective, as presented in Sect. 2.

In order to develop a generalizable unbiased noise-aware method, we rewrite DMD as a two-step procedure: (1) a subspace projection step and (2) an operator identification step. In this form, it becomes simple to show that the subspace projection step introduces a systematic error in existing DMD algorithms when the snapshot data are inexact due to sensor noise and other factors. We propose a modification to the conventional subspace identification step, based on an *augmented snapshot matrix*, in order to remove the source of bias that is systematically introduced into current formulations of DMD. The resulting noise-aware total DMD (TDMD) framework reduces to the standard DMD algorithm when the measured snapshots are without error. Moreover, based on the two-step analysis developed here, the de-biasing procedure is generalizable to other *DMD-like* algorithms that appeal to Koopman spectral analysis, such as optimal mode decomposition [21,58], streaming DMD [26], sparsity-promoting DMD [29], non-uniform DMD [23], and optimized DMD [9]; in such cases, the "operator identification" step is to be replaced by the dynamical analysis algorithm of choice.

After formulating the de-biasing framework in Sect. 2, we study a simple linear system in Sect. 3 to demonstrate the bias resulting from a standard DMD analysis of noisy data; working with a simple linear system, for which the exact solution is known, allows a demonstration and validation of TDMD's ability to converge to the exact spectrum as more and more snapshots are processed. We consider a more representative fluid flow in Sect. 4, where numerical simulation data of laminar flow over a cylinder in two-dimensions is corrupted with synthetic additive Gaussian measurement noise, and compare the performance of DMD and TDMD. Only a *weak* noise signal is added to the numerical data (i.e., high signal-to-noise ratio), such that the resulting bias in the DMD analysis does not significantly alter the interpretation of the identified modes (i.e., the resulting bias in the DMD eigenvalues is small); the example is used to demonstrate that TDMD converges more rapidly (i.e., with fewer snapshots) to the exact (noise-free) spectrum than standard DMD. In Sect. 5, DMD and TDMD are used to extract dynamical information from time-resolved particle image velocimetry (TR-PIV) data of a separated flow. TDMD is found to outperform DMD: TDMD eigenvalues provide an interpretation of the separated flow that is consistent with other analysis techniques, while the associated modes reveal a more detailed description of the spatial structures involved in the dynamics.

We note that our focus here is on measurement noise and data quality, with particular attention on removing the influence of such factors from the ensuing analysis. While TDMD provides a systematic framework for conducting unbiased Koopman spectral analysis in the context of *measurement* noise, further investigation is needed to ensure that such procedures do not remove system-specific *process* noise, characterizations of which can provide descriptive physical insights. An extensive discussion of Koopman spectral analysis for systems exhibiting weak random forcing in the form of process noise can be found in [2]. The influence of process

noise on the Koopman spectrum, as characterized in [2], together with noise-aware techniques like TDMD will be essential to determine the contribution of various noise sources (i.e., data quality versus intrinsic stochastic forcing) on the resulting analysis. Ultimately, TDMD provides a systematic framework for conducting unbiased Koopman spectral analysis in applied settings for which data quality can be an issue; this will be essential for modeling complex systems and extracting credible dynamical descriptions from measured data.

2 An unbiased formulation of dynamic mode decomposition

2.1 Dynamic mode decomposition and Koopman spectral analysis

Consider a dynamical system given by $x \mapsto f(x)$, where $x \in \mathcal{X}$ is the state variable. This evolution law can be expressed in terms of the evolution of an appropriate set of scalar-valued functions of state-space $g : \mathcal{X} \to \mathbb{C}$, known as *observables*. From this perspective, it is useful to consider the *Koopman operator* $\mathcal{K}$, an infinite-dimensional linear operator that maps observables to corresponding observables one step in the future: $\mathcal{K}g(x) = g(f(x))$ [31,37]. The utility here rests in the fact that the dynamics of the *nonlinear* map f can be determined completely from the *linear* Koopman operator.

In recent years, analyzing practical systems via the spectral properties of the Koopman operator (i.e., the eigenvalues, modes, and eigenfunctions of $\mathcal{K}$) has been made possible by means of *DMD-like methods* [8,38,42,55,56], in which one approximates the Koopman operator from data obtained from experiments or simulations, without explicit knowledge of the map f. In these methods, one considers a vector of observables $\psi : \mathcal{X} \to \mathbb{C}^n$ (typically $\mathbb{R}^n$, in practice) evaluated at specific values $x_k \in \mathcal{X}$ and their images $f(x_k)$, for $k = 1, \ldots, m$, and seeks a linear relationship between them:

$$\psi(f(x_k)) = A\psi(x_k), \tag{1}$$

where $A \in \mathbb{R}^{n\times n}$. More specifically, the data consist of pairs of *snapshots* $\psi(x_k)$, $\psi(f(x_k))$, which may be obtained from an experiment, for instance, by taking measurements at two consecutive times. Using the formalism in [50], these snapshots are stored in the $n \times m$ matrices

$$\begin{aligned} X &:= \begin{bmatrix} \psi(x_1) & \cdots & \psi(x_m) \end{bmatrix} \\ Y &:= \begin{bmatrix} \psi(f(x_1)) & \cdots & \psi(f(x_m)) \end{bmatrix}, \end{aligned} \tag{2}$$

and from (1), one seeks a matrix A that satisfies

$$Y = AX. \tag{3}$$

In DMD, A is given by the least-squares/minimum-norm solution to (3):

$$A_{\text{dmd}} := YX^{+}, \tag{4}$$

where X^{+} denotes the Moore–Penrose pseudoinverse of X. It is shown in [50] and [55] that, under certain conditions on the data and observables, the eigenvalues of A correspond to eigenvalues of the Koopman operator $\mathcal{K}$, and Koopman eigenfunctions and modes may be found from A as well. In other words, the methodology above provides a means for conducting Koopman spectral analysis of dynamical systems directly from snapshot data.

2.2 Dynamic mode decomposition, measurement noise, and bias

The above discussion on connections between DMD and the Koopman operator focuses on the *underconstrained* case with "perfect" snapshot data, in which (3) is satisfied exactly, and (4) gives the minimum-norm solution. Indeed, this case is common in many situations with exact snapshot data: for instance, it holds whenever the columns of X (the snapshots) are linearly independent.

Here, we are interested in applying Koopman spectral analysis in practical contexts with imperfect and noisy snapshot data; hence, the underconstrained case is undesirable, as solutions will inevitably overfit the noise. As such, we are primarily interested in the *overconstrained* case, in which we have more snapshots than observables ($m > n$). Note that underconstrained problems can be transformed into overconstrained

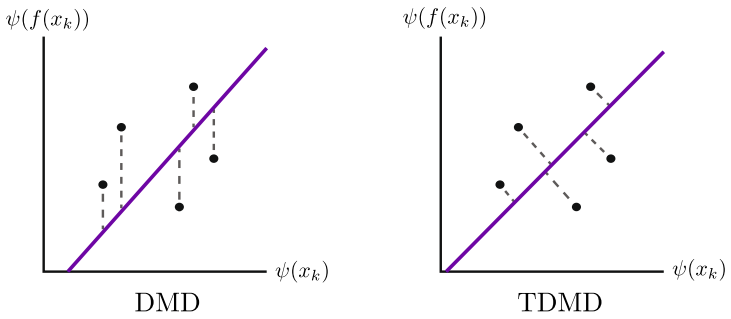

Fig. 1 DMD minimizes error with respect to the time-shifted data $\psi(f(x_k))$ only, thus yielding a biased analysis when the snapshots exhibit measurement noise. In contrast, TDMD minimizes the orthogonal distance between the linear fit and each data point, thus taking all errors into consideration. By accounting for error in *both* $\psi(x_k)$ and $\psi(f(x_k))$, TDMD yields an unbiased analysis

problems via rank-reduction techniques (e.g., POD projection), thus providing a means of managing issues of over-fitting in practice. For example, the original DMD algorithm introduced in [43] projects snapshots onto an r-dimensional subspace (with $r \leq m$) using POD projection. This is particularly important in fluid mechanics applications, since the snapshot dimension is often substantially larger than the number of snapshots that can feasibly be collected in practice. We will discuss subspace projection and rank-reduction later in this section, but for now consider that the overconstrained problem corresponds to the case where (4) represents the least-squares solution

$$\min_{A,\Delta Y} \|\Delta Y\|_F, \quad \text{subject to} \quad Y + \Delta Y = AX, \tag{5}$$

where $\|\cdot\|_F$ denotes the Frobenius norm. (Note that, if the minimizing A is not unique, then (4) selects the solution of minimum norm.) Now, assume the data measurements are corrupted by some noise, which we do not know. One interpretation of (5) is to view Y as the "noisy" snapshots and ΔY as a "noise correction"; DMD then finds a linear relationship between the snapshots X and the "noise-free" snapshots $Y + \Delta Y$.

With this interpretation, it is apparent that the snapshots in X and Y are treated asymmetrically: if we account for noise in the measurements Y, then it seems one should also account for noise in the measurements X and solve the *total least-squares* problem

$$\min_{A,\Delta X,\Delta Y} \left\| \begin{bmatrix} \Delta X \\ \Delta Y \end{bmatrix} \right\|_F, \quad \text{subject to} \quad Y + \Delta Y = A(X + \Delta X). \tag{6}$$

This is the central idea we propose here. We shall see that treating X and Y asymmetrically, as in (5), introduces a *bias* in the eigenvalues of A, even in the context of noisy snapshot data; in contrast, if we account for noise in both X and Y as in (6), then the bias is removed. In fact, as shown in [17] and [51], under certain assumptions on the data and provided that an exact linear relationship (3) between snapshots exists in the noise-free case, then, in the presence of noise, the total least-squares solution converges to the exact solution as the number of snapshots tends to infinity, whereas the least-squares solution does not.

Noise-induced bias in DMD can be understood graphically, as in Fig. 1. Standard DMD seeks a linear fit that minimizes the error with respect to the time-shifted data $\psi(f(x_k))$ *only*; neglecting to account for errors in the unshifted snapshots $\psi(x_k)$ causes the linear fit to be biased away from the solution that would result if the snapshots were noise-free. In contrast, the total DMD (TDMD) perspective considers a minimization in a direction orthogonal to the linear fit—a fact that will become clear in the next section; doing so allows measurement errors in *both* the unshifted and time-shifted snapshots to be considered, thus yielding an unbiased solution.

We emphasize that an asymmetric handling of noise arises in any formulation of DMD that can be reduced to a "one-sided" minimization problem, as in (5); hence, the perspective taken above is equally valid for any such DMD method, and is not restricted to the particular formulation introduced in [50]. For instance, the original DMD algorithm [43] for time series data exhibits this asymmetric handling of noise. The original algorithm adds a "noise correction" term v_{k+1} to each time-shifted snapshot $\psi(x_{k+1})$, whereas the unshifted snapshots $\psi(x_k)$ are left unaltered; of course, this constitutes an asymmetric accounting of measurement noise,

as reflected in (5). In contrast, an unbiased analysis of time series data requires that *both* the unshifted and time-shifted snapshot data must be noise-corrected as,

$$\begin{aligned} X + \Delta X &:= \left[(\psi(x_1) + v_1) \cdots (\psi(x_m) + v_m)\right] \\ Y + \Delta Y &:= \left[(\psi(x_2) + v_2) \cdots (\psi(x_{m+1}) + v_{m+1})\right]. \end{aligned} \tag{7}$$

Although most of the entries in the time series snapshot data matrices X and Y in (7) will be identical—modulo a column-wise shift—all of the entries will exhibit measurement noise contamination that must be accounted for through the noise correction terms ΔX and ΔY. Working with *both* sets of noise-corrected snapshot data, as established in (6), will yield an unbiased analysis.

2.3 A general framework for de-biasing

A de-biased DMD algorithm can be formulated directly from (6) via the singular value decomposition (SVD), as is common in the total least-squares literature [52]; however, a specific SVD-based formulation will not provide useful insights that can leveraged to generalize the de-biasing framework to other DMD-like methods. Here, we present a projection operator interpretation of DMD that makes the de-biasing framework agnostic to the particular formulation of DMD under consideration. As we will show, the solution of (6) can be interpreted as a two-stage procedure: (1) a de-biasing stage followed by (2) an operator identification stage. While simple, this powerful perspective decouples the de-biasing step from the specific formulation of DMD; hence, the two-stage perspective introduced here allows other DMD-like methods to be de-biased as well.

In order to solve the total least-squares problem (6), we appeal to a projection operator perspective [14,15, 59]. Note that (3) may be written equivalently as $X^*A^* = Y^*$, where * denotes Hermitian transpose. Then, the least-squares solution may be obtained by projecting onto the range of X^*. Writing this projection as $\mathbb{P}_{X^*}$ (and noting that orthogonal projections are self-adjoint), we see the least-squares solution A_{ls} satisfies

$$Y\mathbb{P}_{X^*} = A_{\text{ls}} X\mathbb{P}_{X^*}. \tag{8}$$

(Of course, $X\mathbb{P}_{X^*} = X$, but we leave the projection in (8) for analogy with the total least-squares case discussed below.) It is clear that the DMD solution (4) satisfies this relation, noting that $X^+X = \mathbb{P}_{X^*}$. Hence, when the usual DMD algorithm is applied to overconstrained data, one may interpret it as first performing the projections

$$\bar{Y} = Y\mathbb{P}_{X^*}, \qquad \bar{X} = X\mathbb{P}_{X^*} = X, \tag{9}$$

and then finding the minimum-norm solution of $\bar{Y} = A\bar{X}$.

An analogous approach can be used to solve the total least-squares problem (6). First, construct the *augmented snapshot matrix*

$$Z := \begin{bmatrix} X \\ Y \end{bmatrix}, \tag{10}$$

and let Z_n denote the best rank-n approximation of Z (in the Frobenius norm). Then, the solution A_{tls} of (6) satisfies

$$Y\mathbb{P}_{Z_n^*} = A_{\text{tls}} X\mathbb{P}_{Z_n^*}, \tag{11}$$

where $\mathbb{P}_{Z_n^*}$ denotes the projection onto the range of Z_n^*; this may be found from the singular value decomposition of Z, as shown in Step 1 of the algorithm outlined below. The solution of the total least-squares problem may thus be obtained by first projecting the data

$$\bar{Y} = Y\mathbb{P}_{Z_n^*}, \qquad \bar{X} = X\mathbb{P}_{Z_n^*}, \tag{12}$$

and then finding the minimum-norm solution of $\bar{Y} = A\bar{X}$. In practice, one does not need to compute the matrices $\bar{Y}$ and $\bar{X}$ explicitly: in the algorithm given below, we factor the projection $\mathbb{P}_{Z_n^*} = QQ^*$ and compute with the smaller matrices $\hat{X} = XQ$, $\hat{Y} = YQ$.

Both the least-squares and the total least-squares solution approaches described above amount to a single two-stage procedure consisting of (1) a *subspace projection* step, followed by (2) an *operator identification* step, distinguished from one another by the details of the subspace projection step. That is, in the least-squares

formulation (9), only the Y matrix is "corrected" to account for noise, and the correction (projection) depends only on X; in the total least-squares formulation (12), both X and Y are "corrected," and the projection depends on both X and Y. We shall see in the next section that the former approach introduces a bias in the eigenvalues of A when noise is present, while the latter approach does not.

It is worth noting that, if the data matrices do satisfy $Y = AX$ exactly for some A (i.e., if the data are "noise free"), then $\bar{X} = X$ and $\bar{Y} = Y$, for both (9) and (12). (To see this, note that if $Y = AX$, then $\mathcal{R}(Y^*) \subset \mathcal{R}(X^*)$, and hence $\mathcal{R}(Z^*) = \mathcal{R}(X^*)$, which has dimension at most n. Thus, $\bar{Y}^* = \mathbb{P}_{Z_n^*} Y^* = Y^*$ and $\bar{X}^* = \mathbb{P}_{Z_n^*} X^* = X^*$.) In other words, in the absence of noise, both methods are equivalent.

The least-squares and total least-squares problems (5) and (6) arise when the original problem (3) is overconstrained, with $m > n$. However, another common case is when we expect the dynamics to evolve on a low-dimensional subspace, say of dimension $r < n$. As described earlier, in such instances, an underconstrained problem, with $n > m$, can be interpreted as an overconstrained problem when viewed on the low-dimensional subspace, provided that $r < m$; projecting onto an appropriate lower dimensional subspace, with dimension $r < m$, also serves to remedy issues of *over-fitting* that arise when the data are noisy and $n > m$. The usual approach in this situation is to determine a suitable low-dimensional subspace from the data, for instance using POD, to project the snapshots onto this subspace, and then to proceed with (4), where X and Y now contain the projected snapshots [43] (i.e., "projected DMD" as defined in [50]).

It is interesting to note that projected DMD performs a (POD) projection "on the left," in the space of measurements. This projection can serve to "de-noise" the snapshots by retaining only the most energetic content. In contrast, the "exact DMD" algorithm defined in [50] and the de-biased formulation introduced here perform projections "on the right," in the space of snapshots, utilizing $\mathbb{P}_{X_r^*}$ and $\mathbb{P}_{Z_r^*}$, respectively. It is the projection on the right that is responsible for "de-biasing" DMD, when the snapshots are treated symmetrically (i.e., when the projection is computed from both sets of snapshots X and Y). In general, DMD can be performed with projections on both sides (i.e., on the left and on the right), where the appropriate projection operators are determined by considering all of the snapshots (i.e., utilize $\begin{bmatrix} X & Y \end{bmatrix}$ for projections on the left, and $Z = \begin{bmatrix} X^* & Y^* \end{bmatrix}^*$ for projections on the right). Here, we focus on de-biasing—not de-noising—and determine the "best" r-dimensional subspace from a truncated SVD of the augmented snapshot matrix Z only, as described below.

We emphasize that in expressing total least-squares DMD as a two-step process, the subspace projection step (12) can be interpreted as a "pre-processing" step to be used for de-biasing other DMD-like algorithms. Thus, the method may be used with standard implementations of, for example, optimal mode decomposition [21,58], streaming DMD [26], sparsity promoting DMD [29], non-uniform DMD [23], or optimized DMD [9]. For instance, the de-biased algorithm for standard DMD [50] proceeds as follows:

1. Compute the singular value decomposition of Z, and store the first n right singular vectors as columns of a matrix Q. (Then the projection $\mathbb{P}_{Z_n^*}$ is QQ^*, though we will not need this projection explicitly.)
2. Project the snapshot matrices, calculating $\hat{X} = XQ$ and $\hat{Y} = YQ$.
3. Calculate the reduced singular value decomposition $\hat{X} = U\Sigma V^*$.
4. Determine the DMD matrix $\tilde{A}_{\text{dmd}} = U^*\hat{Y}V\Sigma^{-1}$, which is related to the full DMD operator by $\tilde{A}_{\text{dmd}} = U^* A_{\text{dmd}} U$.
5. The DMD eigenvalues λ_i are eigenvalues of $\tilde{A}_{\text{dmd}}$, and the corresponding (projected) DMD modes are $v_i = U\tilde{v}_i$, where $\tilde{A}_{\text{dmd}}\tilde{v}_i = \lambda_i \tilde{v}_i$.
6. If desired, calculate the associated frequency and growth rate for mode i, as $f_i = \angle\lambda_i/(2\pi\delta t)$ and $g_i = \log|\lambda_i|/\delta t$, where δt refers to the time-shift between snapshots stored in X and Y.

(Note that if the dynamics are expected to evolve on an r-dimensional subspace with $r < n$, replace n with r in Step 1 of the algorithm above.)

On a side note, the formulation here allows one to use efficient randomized SVD algorithms [36] to expedite de-biased DMD computations—an option that would not be directly available via a "more traditional" formulation of the total least-squares problem [52]; here, we require the singular vectors associated with the *first* r singular values, rather than those associated with the *last* r singular values. In particular, for the de-biased DMD algorithm above, a significant computational advantage can be gained by leveraging a randomized SVD calculation in Step 1; of course, in such instances, additional care must be taken to ensure that solutions converge with respect to the parameters invoked in a particular randomized SVD implementation. Although the details of randomized SVD methods are outside the scope of this work and are not essential to DMD analysis or the results presented in this study, it is worth mentioning that these methods may be exploited for computational savings in other incarnations of DMD and Koopman spectral analysis as well.

Lastly, the two-stage perspective taken here enables DMD-type methods to be utilized in providing an indication of uncertainties in snapshot data. In particular, for the de-biased DMD formulation proposed here, the "corrected" snapshot data is computed as $\bar{X} = X + \Delta X = X\mathbb{P}_{Z_n^*}$ and $\bar{Y} = Y + \Delta Y = Y\mathbb{P}_{Z_n^*}$, so it follows that the snapshot "error" can be computed as,

$$-\Delta X = X(I - \mathbb{P}_{Z_n^*}), \qquad -\Delta Y = Y(I - \mathbb{P}_{Z_n^*}). \tag{13}$$

The snapshot errors $(-\Delta X, -\Delta Y)$ provide an indication of the uncertainty associated with the snapshot data, without a need to explicitly perform DMD beyond the subspace identification stage. In Sect. 5, we make use of (13) to compare the error fields identified by the noise-aware computations with uncertainties determined by alternative statistical techniques. Such comparisons serve to corroborate the noise-aware framework from the standpoint of snapshot errors and uncertainties.

2.4 Practical considerations

While the total least-squares formulation makes DMD more "robust" to noise—in the sense that the framework explicitly accounts for inexact data and does not systematically introduce bias errors when applied to noisy data—the formulation can also make the solution procedure less stable; total least-squares problems are known to exhibit less stability than least-squares problems, though more robust solution approaches have been developed [16,19,51,52]. While the term *noise-robust* is often used to describe (regularized) total least-squares problems in the literature, in the remainder, we choose to use the term *noise-aware* to emphasize the need for algorithmic techniques with greater computational robustness than may be afforded by the de-biased DMD procedure outlined above. Such issues are outside the scope of this study, but are the focus of ongoing work.

We note that while the noise-aware framework addresses the potential pitfalls associated with measurement noise contamination, the de-biased formulation does not address other practical challenges associated with DMD-based methods. In particular, an assumption that has gone into the formulation here is that the underlying dimension of the low-dimensional dynamics is known, whereas, in reality, this dimension must be determined from the data in some manner. Many past studies have simply allowed the dimensions of the snapshot data to dictate the dimensionality of the DMD representation: Without a rank-reduction procedure, the number of DMD modes and eigenvalues is determined as $\min(m, n)$. At least in the underdetermined case ($m < n$), selecting the number of DMD modes and eigenvalues according to the number of snapshots m that have been collected seems arbitrary. A more judicious choice would be to truncate to a lower rank, if appropriate, as indicated by some other metric, as outlined below; otherwise, the analysis will be based on an over-fitting of noisy data. Such has been the impetus for the development of optimal mode selection techniques [9,21,29,58].

One option available to the practitioner in determining an appropriate low-dimensional DMD representation is to impose a larger truncation level than expected during the DMD computation, followed by an optimal mode selection technique, such as sparsity-promoting DMD [29]; however, we note that these propositions must be explored further, as previous investigations have indicated a sensitivity of total least-squares solutions to over-estimation of the "correct" truncation level [48]. A simpler alternative, commonly employed in the literature, is to determine the dimension of a low-order representation from a spectral gap (if one exists) based on a POD analysis of the snapshot data. Even when the POD analysis does not reveal a spectral gap, an appropriate truncation level can be determined through the use of conventional model selection methods—already established in the context of numerical analysis and system identification—such as, e.g., Akaike Information Criterion [1], generalized cross-validation [18], Morozov's discrepancy principle [39], or L-curve [24]. Model selection techniques have proven valuable in a number of contexts to systematically overcome over-fitting issues and for addressing problems of bias-variance trade-off. For the purposes of the current study, we do not consider optimal rank selection procedures; instead, we are interested in comparing the standard and noise-aware DMD methods directly, and compare performance for a set of truncation levels where appropriate. In Sect. 3, we also investigate the influence of over-truncation and under-truncation on DMD-based spectral analysis.

To distinguish the unbiased formulation from standard DMD in the remainder of the manuscript, we refer to this noise-aware framework as TDMD, owing to its relationship with total least-squares. In the following sections, we demonstrate the effectiveness of TDMD on a series of large-scale dynamical systems with noise-contaminated snapshot data.

3 DMD on linear systems

In order to highlight the ability of TDMD to yield unbiased approximations of the underlying dynamics in the context of noisy data, we consider a simple model problem for which the exact solution is known: a low-dimensional linear system with a large number of noisy observables. The linear system considered here has no particular physical relevance; rather, it is a simple example designed to convey our key point: measurement noise causes DMD to over-predict the damping of dynamic modes—even in the case of simple linear dynamics—whereas TDMD yields an unbiased characterization of the dynamics. Incorrect estimates of the damping associated with various modes can have deleterious consequences on reduced order models formulated around timescale arguments. Further, in some circumstances, biased estimates can lead to false conclusions regarding the stability of modes. Indeed, an unstable mode could potentially appear stable from the standpoint of a standard DMD-based analysis—a consequence of unphysical noise-induced damping.

In particular, we consider a linear system composed of three dynamic modes with associated eigenvalue pairs $\lambda_1 = \mathrm{e}^{(\pm 2\pi i)\delta t}$, $\lambda_2 = \mathrm{e}^{(\pm 5\pi i)\delta t}$, and $\lambda_3 = \mathrm{e}^{(-0.3\pm 11\pi i)\delta t}$, with $\delta t = 0.01$ s. Note, the third mode is slightly damped, whereas the other two are purely oscillatory. The observables are generated as a randomly chosen linear transformation from $\mathbb{R}^6$ to $\mathbb{R}^{250}$ (i.e., $n = 250$, $r = 6$). The corresponding snapshots are corrupted by additive zero-mean Gaussian noise $\mathcal{N}(0, 0.05)$. Both standard and TDMD are performed on time series data with $m = \{100, 200, 500\}$ snapshot pairs. Each method is repeated for 200 independent realizations of the data, all generated from a different randomly selected initial condition for each state variable $\mathcal{N}(1, 0.1)$ and a different noise sequence. The resulting spectra are compared in Fig. 2. Note that the signal-to-noise ratio associated with the damped mode will diminish with time. An ensemble of shorter snapshot sequences can be used to overcome the issue of weakening signal-to-noise ratio. However, since time series data are commonly used in practice, we present the time series results here.

Even with a subspace projection to the known dimension of the underlying dynamics ($r = 6$), standard DMD yields a biased determination of the growth/decay characteristics. The frequencies identified by standard DMD possess a degree of bias as well. This example highlights the potential pitfalls of previously employed "noise-mitigation" procedures such as ensemble averaging and cross-validation; DMD possesses bias in an expected value sense, so while such methods will reduce the variance, they will not remove the bias error. In contrast, the unbiased TDMD formulation quickly converges to the correct spectrum, in an expected value sense, also with a decreasing variance as the number of collected snapshots increases. Thus, in this example, TDMD correctly classifies the modes as stable/unstable and predicts the associated frequencies correctly as well. This suggests that commonly employed noise-mitigation techniques (e.g., ensemble averaging) can be applied with greater confidence in the TDMD setting.

Of course, the degree of bias is related to the signal-to-noise ratio. Under favorable noise conditions [11], the resulting bias due to noise will not alter the dynamical interpretation of particular modes. Nonetheless,

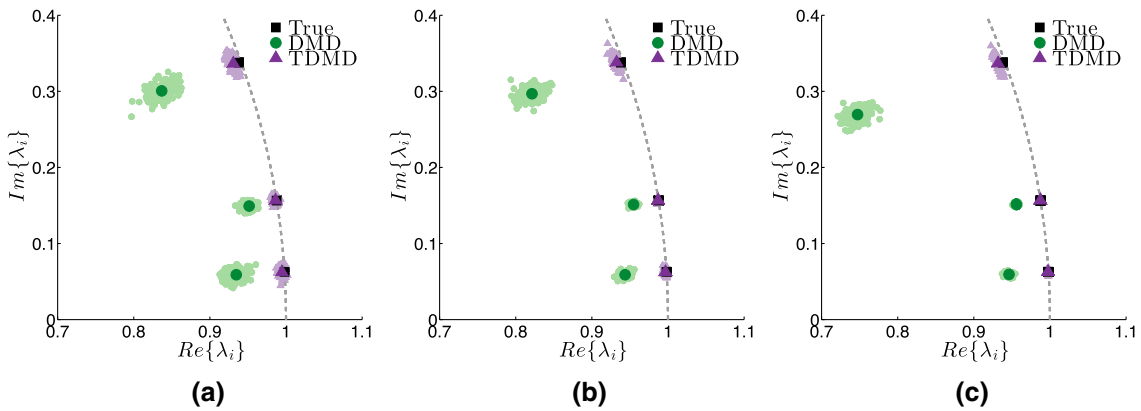

Fig. 2 Spectrum for a linear system. As the number of snapshots m increases, the spectrum predicted by TDMD converges with essentially no bias and slightly tighter variance compared with standard DMD. Each snapshot has dimension $n = 250$ and is corrupted by zero-mean Gaussian noise $\mathcal{N}(0, 0.05)$. All results are computed with $r = 6$. The true eigenvalues (*black squares*) are plotted along with the mean values from standard DMD (*dark circles*) and TDMD (*dark triangles*) based on 200 different noise-realizations. The eigenvalues from each of the individual realizations of standard DMD (*light circles*) and TDMD (*light triangles*) indicate the variance associated with each method. **a** $m = 100$. **b** $m = 200$. **c** $m = 500$

even in such circumstances, TDMD seems to converge to the correct spectrum more rapidly than standard DMD, as will be demonstrated in the next section.

The above analysis on noise-induced bias assumes that the true system rank is known a priori, but in practice this is seldom the case. Indeed, over- and under-truncation are quite likely to arise when performing DMD-based analyses. Here, we will investigate the role of over- and under-truncation on DMD/TDMD spectra for a *single realization* of the noisy data analyzed in Fig. 2a, with $m = 100$. This case corresponds to the underconstrained scenario that is typical of fluids datasets.

DMD/TDMD spectra for various truncation levels are reported in Fig. 3. Tiles (a)–(d) demonstrate that over-truncation—i.e., selecting r to be less than the true system rank—can give rise to misleading spectra, as may be expected of an analysis that discards signal along with noise. With over-truncation, DMD and TDMD both consistently capture a single mode for various values of r; however, the other identified eigenvalues vary substantially between truncation levels. In contrast, under-truncation—i.e., selecting r to be greater than the true system rank—tends to capture all three modes associated with the true system modes fairly consistently, as seen in tiles (e)–(g). The DMD eigenvalues associated with these three modes are damped relative to the true eigenvalues, whereas the associated TDMD eigenvalues are comparably more accurate. However, in both DMD and TDMD, under-truncation inevitably yields spurious eigenvalues, as an artifact of "fitting the noise." These spurious modes are found to be substantially damped at higher truncation levels (i.e., lower r values), but approach the unit circle as truncation level decreases (i.e., r increases). In the case of no truncation (i.e., $r = m = 100$), DMD and TDMD yield the same spectra (see tile (h)). In this case, the majority of spurious eigenvalues lie on the unit circle, making it difficult to discern relevant modes from irrelevant modes. Further, without truncation, both methods fail to capture one of the true modes. This observation corroborates the point that rank-reduction should be performed when the underlying system dimension is less than the number of observables and the data are noisy with $m < n$.

Determination of a suitable truncation level for DMD-based analysis is clearly an important problem, as illustrated in this simple example. Various systematic approaches for determining a suitable truncation level were discussed in Sect. 2. In the remaining sections, our focus is on eliminating noise-induced bias in DMD-based methods, so we resort to using a simple rank determination strategy based on POD energy retention arguments. This approach provides a systematic means of evaluating DMD/TDMD performance on noise-corrupted data, without introducing additional parameters that could make comparison dubious. Still, further investigation and development of reliable methods for rank determination is warranted—even in settings with *noise-free* data.

Sample MATLAB code for this example is available as supplementary material.[1]

4 DMD on cylinder flow simulations

While the demonstration of TDMD on a linear system showcases the advantages of the unbiased formulation over standard DMD in the simplest of cases, TDMD outperforms standard DMD in the analysis of more complex systems as well. Here, we will study both DMD and TDMD in the context of fluid flows by considering numerical simulations of the canonical problem of flow past a cylinder, with synthetic noise contamination; actual experimental datasets are considered in the next section. Our main objective with this numerical example is to highlight the advantages of TDMD over DMD, even in situations for which the bias in DMD eigenvalues becomes negligible as the number of snapshots increases. As such, we consider *mild* noise contamination through the use of a simplistic model of noisy flowfield data. In particular, this example shows that TDMD converges to the exact spectrum more rapidly than standard DMD, even when the DMD bias is negligible as the number of snapshots increases; that is, TDMD requires fewer snapshots than standard DMD to yield converged descriptions of the dynamics, even in scenarios for which sensor noise is minimal.

Vorticity data, as reported in [26], generated via direct numerical fluids simulations (DNS) and sampled at a rate of $f_s = 100$ Hz ($\delta t = 0.01$ s) are considered in this demonstration to ensure full control over (synthetic) measurement noise; the Reynolds number based on cylinder diameter is $Re = 100$. To establish a baseline set of true DMD eigenvalues and modes, standard DMD is first applied to the set of exact snapshots (i.e., no noise corruption). Next, the effect of measurement noise is considered by adding zero-mean Gaussian sensor noise $(\Delta X, \Delta Y) \sim \mathcal{N}(0, 0.001)$ to the exact vorticity snapshot data $(\bar{X}, \bar{Y})$. The effect of the number of snapshots m is studied by concatenating the original dataset ($n = 59{,}501$, $m = 116$) with itself, but with different realizations of additive measurement noise; here, cases with $m = \{116, 232, 464\}$ are considered.

[1] See supplementary material for a MATLAB example and implementation of TDMD.

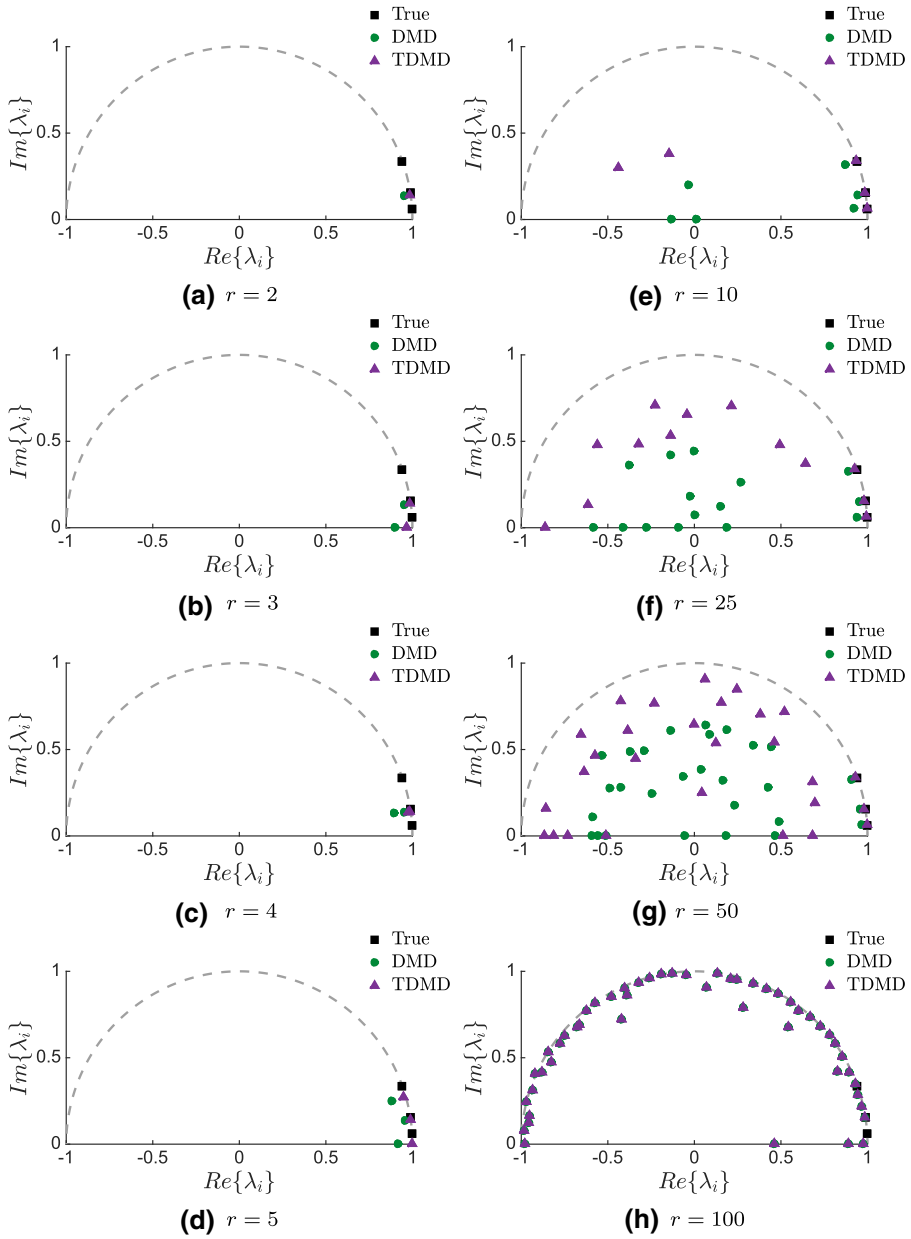

Fig. 3 Influence of truncation level on spectra. Over-truncation leads DMD/TDMD to partially resolve the correct spectrum, as in tiles **a**–**d** for which the imposed rank is less than the true system rank of $r = 6$. Under-truncation, as in tiles **e**–**g**, tends to capture relevant spectra, at the cost of introducing (damped) spurious eigenvalues that are misleading and can potentially obscure subsequent analysis. Without any truncation ($r = m = 100$), DMD and TDMD yield the same spectra, which consists of a large number of undamped spurious modes, as in tile **h**. Note that without truncation, both DMD and TDMD fail to capture one of the true eigenvalues that is always captured in cases of under-truncation. The analyses here are based on a single snapshot realization of the data used in Fig. 2a

The rank-reduction level $r = 21$ is determined by seeking to retain over 99% of the energy content based on the SVD of the noise-corrupted data stored in X. By construction of this example, the computed DMD spectrum is not significantly altered by the noise—i.e., most of the DMD eigenvalues coincide with the true eigenvalues (see Fig. 4). Even so, TDMD is able to handle the noise contamination more effectively; as the number of snapshots is increased, TDMD converges to the true spectrum more quickly than standard DMD. Further discussion of DMD convergence rates and bias levels can be found in the complementary work of Dawson et al. [11].

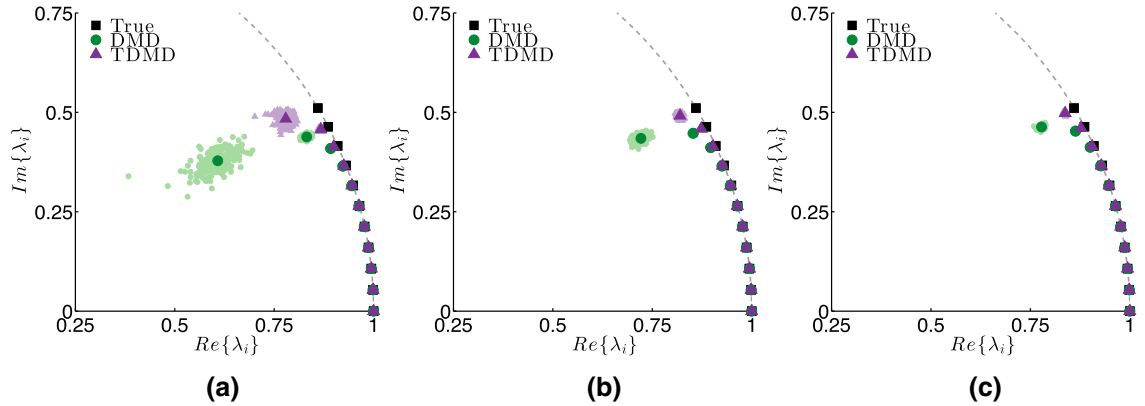

Fig. 4 Spectrum for the flow over a cylinder (DNS). The spectrum predicted by TDMD converges to the true spectrum more quickly than standard DMD as the number of snapshots m increases. Here, each snapshot is corrupted by zero-mean Gaussian measurement noise $\mathcal{N}(0, 0.001)$, each snapshot has dimension $n = 59{,}501$, and both methods set $r = 21$. The true eigenvalues (*black squares*) are plotted along with the mean values from standard DMD (*dark circles*) and TDMD (*dark triangles*) based on 200 different noise-realizations. The eigenvalues from each of the individual realizations of standard DMD (*light circles*) and TDMD (*light triangles*) indicate the variance associated with each method. **a** $m = 116$. **b** $m = 232$. **c** $m = 464$

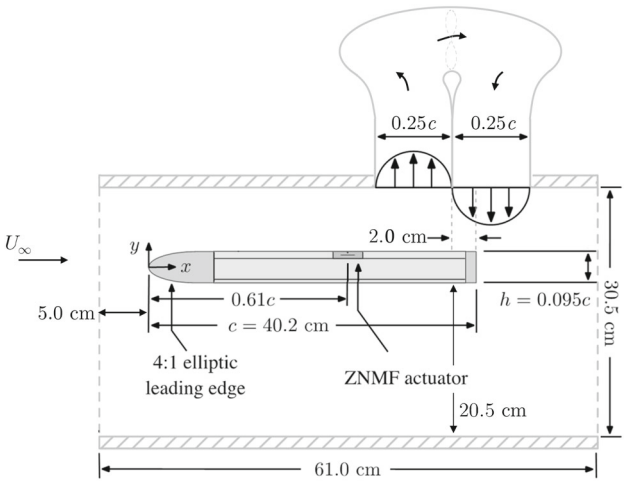

Fig. 5 Schematic of the wind tunnel test section for the separated flat plate experiments. Flow separation is generated by imposing an adverse pressure gradient through a blowing-suction boundary condition on the test section ceiling

5 DMD on flow separation experiments

TDMD's ability to extract the correct spectrum from synthetically corrupted numerical data garners trust for its use as a reliable method for fluid flow analysis; however, the assumptions of additive Gaussian measurement noise considered in our numerical study may be overly idealized. Further, the mild level of noise contamination may not be representative of practical realities in physical experiments. A more compelling demonstration of TDMD's utility for noise-aware dynamical systems analysis can be made by working with noisy real-world data collected from a physical experiment. As such, we now consider an experiment of separated flow over a flat plate, conducted in the Florida State Flow Control (FSFC) wind tunnel (see Fig. 5). The specific flow configuration studied here is expected to exhibit persistent undamped dynamics; based on the results of our previous examples, this suggests that TDMD may prove to be a better candidate for analysis than standard DMD.

The FSFC is an open-return wind tunnel with test section area of 30.5 cm $\times$ 30.5 cm and a length of 61.0 cm. The chord of the plate is $c = 402$ mm, the span is $s = 305$ mm, and the height is $h = 0.095\,\mathrm{c}$ (see Fig. 5). The leading edge profile of the plate is a 4:1 ellipse and the trailing edge is rectangular.

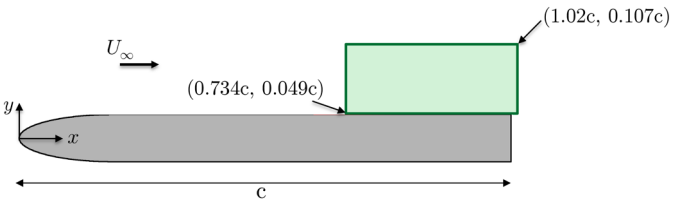

Fig. 6 The measurement plane, depicted by the shaded box in this schematic, is oriented streamwise and *vertical*, grazing the top surface of the flat plate

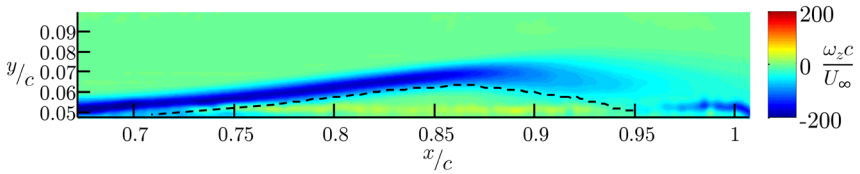

Fig. 7 Average z-vorticity as computed from TR-PIV snapshots. The line of $\bar{u} = 0$ is the *black dashed line*

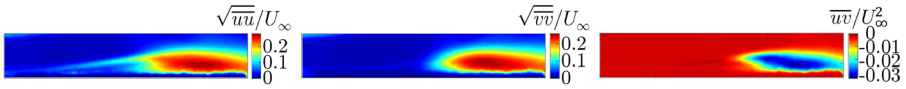

Fig. 8 The turbulence statistics, computed from the snapshot data, indicate increased fluctuations in the shear layer, downstream of the separation point. The x and y limits for these measurement windows are the same as in Fig. 7

The freestream velocity is set to $U_\infty = 3.9$ m/s such that the chord Reynolds number is $Re_c = 10^5$. To generate the separation of the laminar boundary layer, an adverse pressure gradient is generated by suction/blowing on the ceiling of the wind tunnel test section. The blowing/suction is maintained by a closed return duct system mounted on the ceiling of the test section, by which a portion of the free stream is siphoned off and ducted back into the flow further downstream. This is made possible by a variable speed fan mounted within the separation system duct. The fan speed is adjusted such that the maximum suction velocity through the entrance of the duct is $0.32U_\infty$, and the maximum blowing velocity at the outlet is $0.31U_\infty$.

Time-resolved particle image velocimetry (TR-PIV) measurements of the separated flow are acquired by synchronized high speed laser and camera equipment. The measurement plane is oriented in the $x - y$ plane, grazing the top surface of the flat plate (see Fig. 6). Snapshots of the velocity field ($n = 19{,}778$, $m = 6000$) are sampled at a rate of $f_s = 1600$ Hz ($\delta t = 0.625$ ms). The velocity vectors are determined by computing the cross-correlation between recursively smaller windows of the PIV image pairs. The final window size is 16×16 pixel, with an overlap of 75%, resulting in a final vector resolution of 8.9 vectors per mm.

The extent of the separation region is illustrated in Fig. 7 by the line of $\bar{u} = 0$, depicted as the black dashed line, which is superposed on contours of mean vorticity. The length of the mean separation bubble is found to be $L_{\text{sep}} = 0.228\,\text{c}$. Turbulent statistics are computed from the TR-PIV snapshots and provided in Fig. 8 as contours of the standard deviation and covariance of the u and v velocity components. These plots show that fluctuation levels increase dramatically in the transitioning shear layer, downstream of the separation point. This, along with the apparent thickening of the mean shear layer (Fig. 7), indicate enhanced turbulent mixing in this region. DMD analysis of this data, presented later, suggests that multiple modes are responsible for the evolution of the laminar boundary layer into the high-fluctuation regions.

To further investigate the nature of the velocity field fluctuations, flow velocity time series for specific points are extracted from the PIV measurements. These probe locations are oriented along the mean shear layer and within the recirculation region (shown in Fig. 9). A total of six probe time series are extracted. Power spectral density (PSD) estimates for these probe data are computed using Welch's method [3] for a block size of 800 samples, resulting in a frequency binwidth of 2 Hz. These data are determined to be statistically stationary with 98% confidence by the reverse arrangement test [3].

The power spectra are plotted with respect to frequency in Fig. 10. The increased turbulent fluctuations are evident in Probes 2, 3, and 4 as increased broadband content with respect to that of Probe 1. However, all of the probes exhibit distinct frequency peaks at $f = 108$ Hz and $f = 120$ Hz. This suggests that the phenomena responsible for these oscillations are global in nature, and are resilient throughout the turbulent region. These characteristics indicate that DMD is a suitable analysis approach for these flow data.

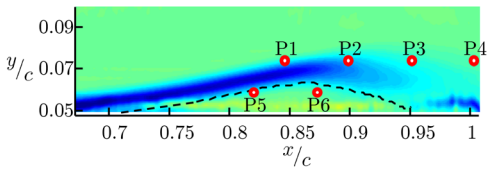

Probe	x/c	y/c	z/c
P1	0.84	0.072	-0.11
P2	0.90	0.072	-0.11
P3	0.96	0.072	-0.11
P4	1.01	0.072	-0.11
P5	0.82	0.058	-0.11
P6	0.87	0.058	-0.11

Fig. 9 Velocity probe locations plotted with respect to the mean vorticity field. Probes 1 through 4 are oriented *horizontally* through the shear layer, and probes 5 and 6 are embedded within the recirculation region

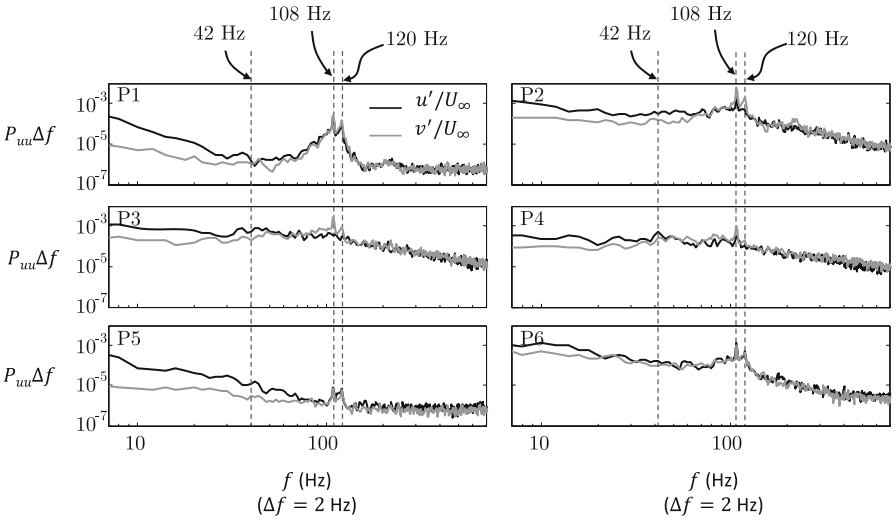

Fig. 10 Power spectra of the velocity values extracted from the PIV fields at the points shown in Fig. 9. The data are mean subtracted and normalized by the freestream velocity. High amplitude peaks are highlighted

We now turn attention to DMD and TDMD for analysis of the TR-PIV snapshot data. Recall that without truncation in situations for which the snapshot dimension is larger than the number of snapshots, both methods will overfit the data and give identical results. Here, DMD and TDMD are performed for three different truncation levels; specifically, we set $r = \{10, 25, 35\}$, which correspond to retaining, respectively, 95.0, 95.5, and 95.6% of energy content based on an SVD of X. Spectra and mode amplitudes for each of these r values are presented in Fig. 11, where the mode amplitudes are computed based on all snapshots—as in [29]—and normalized with respect to the maximum amplitude. Note that the frequencies associated with the modes determined by TDMD are relatively consistent for each of the truncation levels, whereas the DMD frequencies seem to be less consistent. For instance, all three of the TDMD results show a dominant mode with a frequency of approximately 40 Hz—a mode that *weakly* appears in the power spectra analysis (see Fig. 10); however, DMD only identifies this same mode for $r = 10$, and no longer extracts it for larger values of r.

As seen in Fig. 11a–c, the dominant oscillatory modes extracted via TDMD are much less damped than those identified by standard DMD. For larger r, the damping of the DMD modes increases, revealing a clear sensitivity to truncation level. Interestingly, both methods identify lightly damped modes in the frequency range 100–120 Hz, which corresponds to the most prominent frequency peak in the power spectra; this is the only mode that standard DMD consistently places close to the unit circle. On the other hand, TDMD consistently picks out the mode in the 100–120 Hz range, as well as other lightly damped modes, which appear as minor peaks in the power spectra of Fig. 10. The extraction of lightly damped modes by TDMD is consistent with the fact that the data are statistically stationary, as reported earlier. Although neither method identifies a mode at exactly 120 Hz for the truncation levels reported here, the 120 Hz mode is identified for larger truncation values r. However, as the truncation level increases, the influence of noise becomes stronger: More spurious modes appear in the analysis, and all identified modes exhibit greater damping. These observations seem to suggest that the peaks in the power spectra at 42 and 108 Hz (see Fig. 10) may be more "dynamically significant" than the one at 120 Hz. To make such claims with greater confidence would require an objective

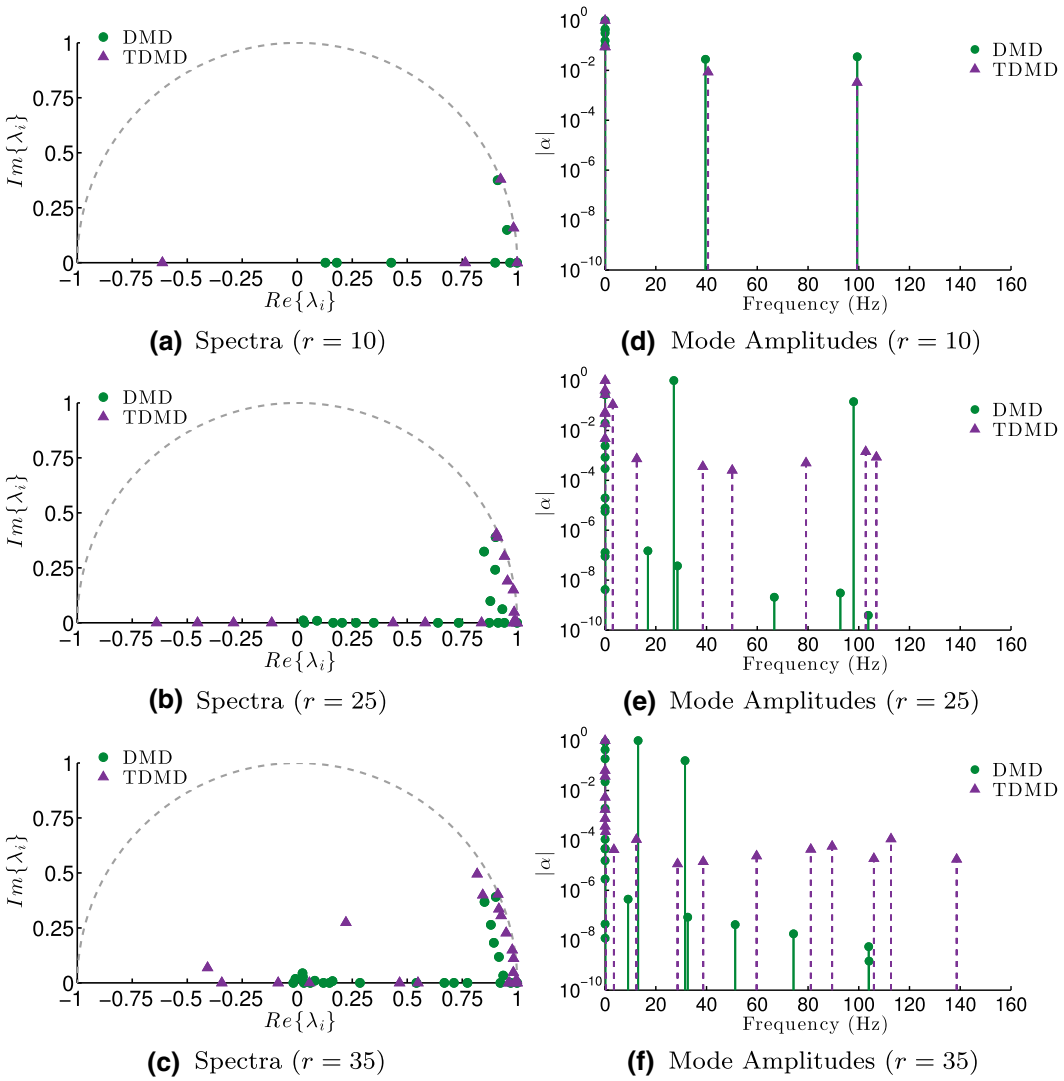

Fig. 11 TDMD predicts modes with less damping than those predicted by DMD; further, TDMD predictions remain more consistent for various truncation values. Spectra for $r = \{10, 25, 35\}$ are presented in (**a**–**c**). Mode amplitudes are normalized by the maximum amplitude and plotted versus frequency for $r = \{10, 25, 35\}$ in (**d**–**f**)

and reliable means for optimal rank selection in the context of noisy datasets; at the moment, this important issue remains unresolved.

In addition to the temporal characteristics of modes determined through the DMD eigenvalues, the spatial structure of each mode is of interest as well, especially when one is interested in gaining physical insights from DMD-based analysis. The real components of the dominant oscillatory vorticity modes—computed as the curl of DMD/TDMD velocity modes—are plotted in Figs. 12 and 13 for $r = 10$ and $r = 25$, respectively; the modes for $r = 35$ are excluded here for brevity. The mode shapes extracted for $r = 10$ are quite similar between standard DMD and TDMD, though the modes identified by TDMD appear less grainy, especially near the upper and lower regions of inflow to the PIV window. The differences in modes computed by the two methods is much more pronounced for $r = 25$ (see Fig. 13). TDMD identifies spatial structures that standard DMD either captures in less detail or misses completely. As one may suspect from the mean flow visualization and Fig. 7, much of the dynamic activity occurs in the vicinity of the separation bubble (e.g., compare active regions in the modes to the mean flow in Fig. 7). In particular, TDMD reveals a set of modes with notable structural complexity that combine dynamically to drive the dynamics observed in the shear layer and separation bubble. Future studies will need to be performed with snapshot data from the wake region downstream of the plate included as well; such studies are necessary to uncover additional dynamical interplays between these various regions of the flow.

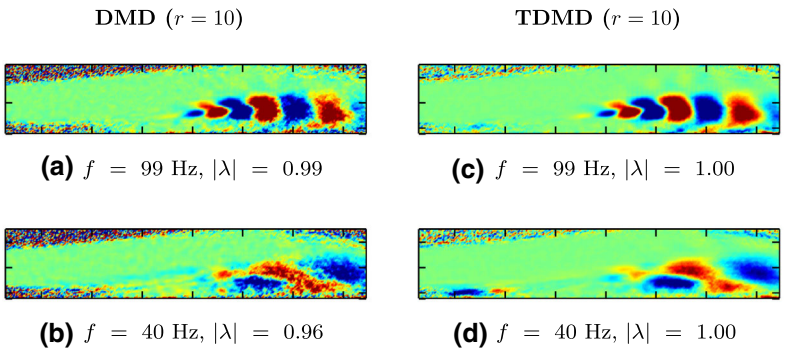

Fig. 12 The spatial structures associated with the oscillatory modes identified by DMD/TDMD with $r = 10$ in Fig. 11a, d appear to be consistent with one another; however, the standard DMD modes in tiles (**a**, **b**) exhibit a larger degree of noise contamination, and the dynamics exhibit larger damping. Here, modes of vorticity are computed from DMD/TDMD modes of velocity. Plots (**a**, **b**) correspond to DMD, and plots (**c**, **d**) to TDMD

TDMD outperforms standard DMD in a number of ways in the analysis of the separated flow: e.g., in contrast to standard DMD, TDMD yields consistent results for various values of r and also extracts modes that more clearly expose detailed spatial structures associated with the active regions of the flow and appear to be less grainy. The primary factor in TDMD's superior performance is an unbiased treatment of snapshot *error* in the framework—recall, standard DMD implicitly treats $\Delta X = 0$. Since error is a large part of the TDMD formulation, it seems natural to look more closely at the errors identified by TDMD. Recall that the subspace projection stage serves to de-bias DMD by appropriately accounting for additive snapshot errors $(-\Delta X, -\Delta Y)$, which can be computed directly via (13)—i.e., $-\Delta X = X(I - \mathbb{P}_{Z_n^*})$ and $-\Delta Y = Y(I - \mathbb{P}_{Z_n^*})$. These error fields, which are typically not computed in practice, can be compared against uncertainty fields computed by alternative statistical methods to provide a qualitative validation of TDMD from the standpoint of the errors.

For the current study the correlation statistics method for determining PIV uncertainty [54] is employed due to its utility and current implementation in the PIV vector calculation in the LaVision DaVis software. This method provides an estimate of the random uncertainty of PIV velocity vectors at every grid point, for each snapshot. Central to the correlation statistics method for uncertainty is the assumption that the converged correlation function between a PIV image pair is symmetric about the maximum. Therefore, the uncertainty is determined by the observed asymmetry in the correlation function [54]. The asymmetry is defined as the difference between corresponding side lobe levels of the computed correlation. Relating this to measurement error is done by computing the residual velocity that results from the asymmetry, then the standard deviation of the residual velocity is estimated from each elemental contribution to the asymmetry within an interrogation window.

Figure 14 contains filled contours of the uncertainty for select snapshots with black contour lines depicting the error field identified by the TDMD projection. The overlapping contours indicate that the error identified by the TDMD projection coincides with the regions of high uncertainty. Note that the measurement error is increased within areas of increased turbulent mixing. A notable result from the works by Wilson and Smith [57] and Timmins et al. [49] is that instantaneous velocity gradients exhibit the largest contribution to measurement uncertainty. This is the most likely explanation for the elevated errors in this region.

The root-mean-squared value of the error fields identified by the TDMD subspace projection is compared with the uncertainty of the mean of the PIV snapshots in Fig. 15. The uncertainty of the mean flow is determined by propagating the uncertainty from the snapshot uncertainties determined by correlation statistics method. These are computed for all 6000 snapshots, which provides a statistical measure of the error identified by the different methods. By the inherent differences between the methods, it is not expected that Fig. 15a, b will match quantitatively. Nevertheless, qualitative agreement is identified in the high-error regions. For example, both results show that higher error is expected downstream of the separation point, within the high-fluctuation region. Additionally, both methods indicate that the u-component of the measurements exhibit higher error than the v-component in the shear layer.

From this study of flow separation using TR-PIV data, it appears that TDMD offers valuable advantages over standard DMD. The errors computed by TDMD are qualitatively similar to the snapshot uncertainties determined by alternative methods, and most importantly, this error is accounted on *all* snapshots in the

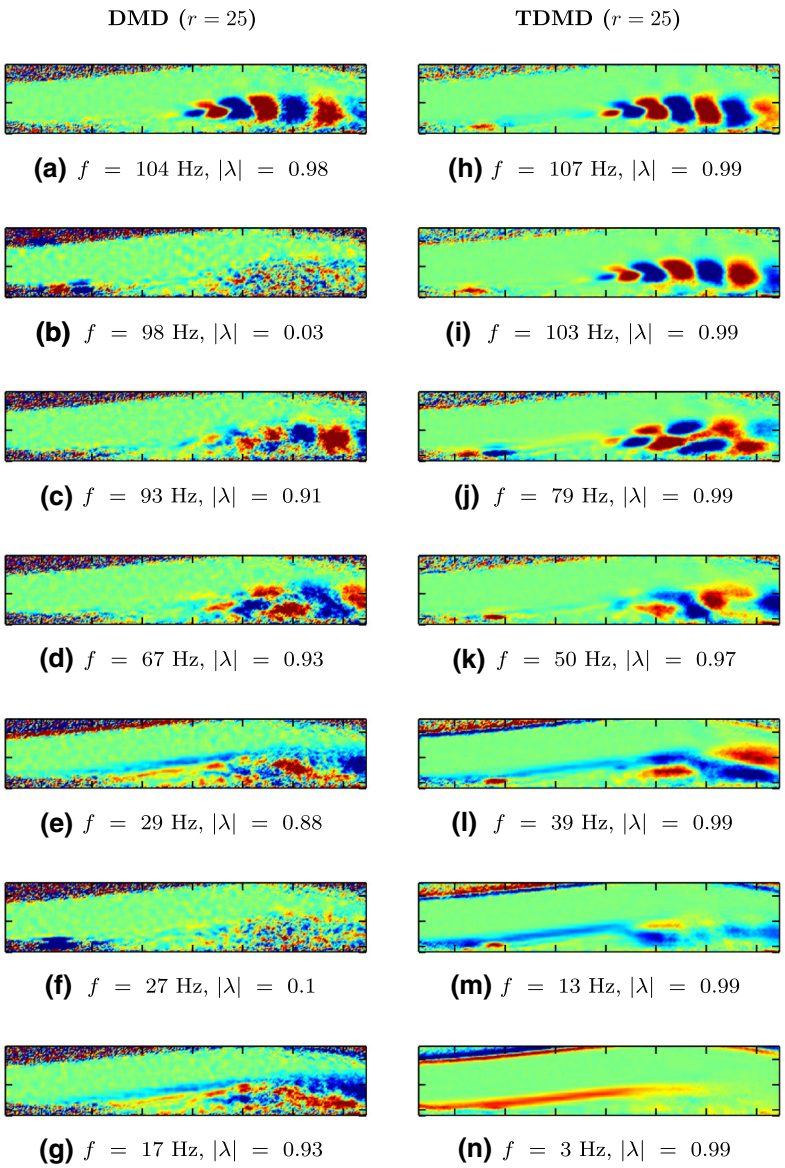

Fig. 13 A comparison of the spatial structures associated with the oscillatory modes reported in Fig. 11b, e suggests that some aspects of the separated flow may be characterized by different dynamics than revealed by standard DMD. All of the spatial structures extracted by TDMD exhibit a clear coherence; in contrast, structures extracted by DMD show artifacts of noise contamination—especially apparent in tiles (**b**, **f**). Here, $r = 25$ and modes of vorticity are computed from DMD/TDMD modes of velocity. The oscillatory vorticity modes are plotted top to bottom in order of decreasing frequency for DMD (**a**–**g**) and TDMD (**h**–**n**)

algorithm formulation. Doing so removes the bias in the eigenvalues, allowing TDMD to identify lightly damped modes as such—in contrast to standard DMD. Further, the de-biasing nature of TDMD also seems to improve the quality of the identified modes, revealing detailed spatial structures that are missed by standard DMD. Lastly, although additional study is required to develop reliable methods for optimal rank selection, we note that in the present analysis TDMD yields results that are more consistent between truncation levels than standard DMD.

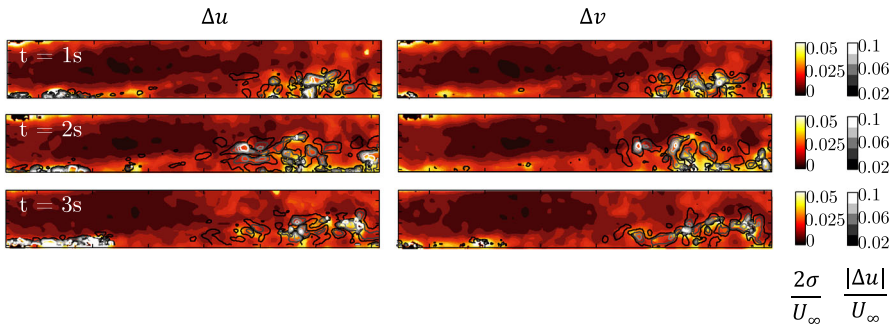

Fig. 14 The error field associated with the TDMD pre-processing step indicates that most of the "data corrections" are made in the same spatial regions of high data uncertainty, as estimated from the correlation statistics method of the TR-PIV data [54]. The shaded contours correspond to the 95% uncertainty bounds as quantified by Wieneke's method (*light* regions have greater uncertainty than *dark* regions), while the *gray contour lines* correspond to the error field computed in the TDMD pre-processing stage, $|\Delta X|$, normalized by the freestream

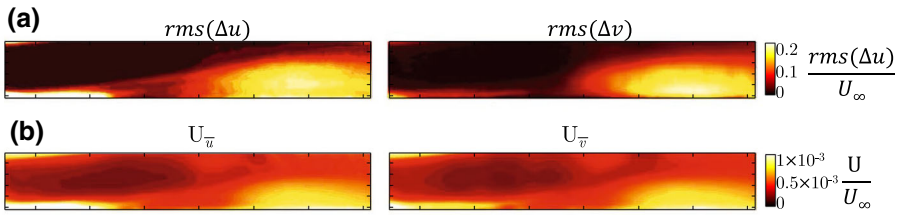

Fig. 15 Comparison of (**a**) the root-mean-squared value of the error fields identified by the TDMD subspace projection with (**b**) the uncertainty of the mean of the PIV snapshots from the correlation statistics method. Calculations are based on a sequence of 6000 snapshots. Despite the differences between the methods there is relative agreement in the identified high-error regions

6 Concluding discussion

By representing DMD as a two-stage process, we have identified an asymmetric treatment of snapshot data in standard formulations of DMD. As a result, we have isolated the source of noise-induced error in DMD that has previously been observed and reported in the literature. Importantly, our determination of this error as a systematically introduced bias indicates that commonly employed approaches to "de-noising," while reducing the variance in the resulting DMD analysis, will inevitably yield biased results; the systematic introduction of bias errors cannot be removed by various methods for averaging and cross-validation. Instead, we propose forming an augmented snapshot matrix (10)—as in problems of total least-squares—in order to account for the errors present in *all* of the available data during the subspace projection step; in doing so, one removes the systematic introduction of error and arrives at an unbiased formulation of DMD.

Although TDMD addresses issues of noise-induced bias, other practical considerations and outstanding issues surrounding DMD-based methods—discussed in Sect. 2—still remain to be resolved. While the formulation proposed here is unbiased, further study is needed to robustify computational analysis techniques; total least-squares problems are known to exhibit numerical sensitivity due to their "de-regularizing" nature [16,19,51,52]. The de-biasing procedure presented generalizes to other *DMD-like* algorithms as well; one need only apply the subspace projection step, and then replace the "operator identification" step by the algorithm of choice (e.g., optimal mode decomposition [21,58], streaming DMD [26], sparsity-promoting DMD [29], non-uniform DMD [23], or optimized DMD [9]). Despite these gains, techniques for distinguishing between measurement and process noise are still needed.

In addition, subspace projection and rank-reduction are key ingredients for DMD analysis of noisy snapshot data measured from fluid flows. In TDMD, this projection is found by accounting for *all* of the snapshots, which removes the bias introduced by previous formulations of DMD. However, as in standard DMD, determination of this projection is accompanied by an implicit assumption that the truncation level is known ahead of time. Though numerous studies have proposed various techniques for selecting an appropriate truncation level or set of modes, the notion of optimal rank determination remains an open question and very well may depend on context. Despite the progress that still needs to be made in this regard, TDMD offers a powerful perspective for pursuing Koopman spectral analysis in the context of measurement uncertainty.

The availability of an unbiased DMD framework will be essential to performing valid data-driven Koopman spectral analysis in practical real-world contexts with imperfect snapshot measurements. By invoking the two-stage TDMD framework, Koopman operator descriptions of a dynamical system determined from experimental data can be regarded with greater confidence, which will ultimately enable more accurate dynamical descriptions of complex time-evolving systems. Moreover, forecasts of future system behavior from TDMD models will be more representative than those based on standard DMD models, since TDMD models will be able to ascertain the correct trends from past data, even when the data are noisy or imprecise.

Acknowledgements The authors thank Scott T.M. Dawson and Matthew O. Williams for insightful discussions about DMD methods for Koopman spectral analysis.

References

1. Akaike, H.: A new look at the statistical model identification. IEEE Trans. Autom. Control **19**(6), 716–723 (1974)
2. Bagheri, S.: Effects of weak noise on oscillating flows: linking quality factor, floquet modes, and Koopman spectrum. Phys. Fluids **26**, 094104 (2014)
3. Bendat, J.S., Piersol, A.G.: Random Data: Analysis and Measurement Procedures, vol. 729. Wiley, New York (2011)
4. Berger, E., Sastuba, M., Vogt, D., Jung, B., Ben Amor, H.: Estimation of perturbations in robotic behavior using dynamic mode decomposition. Adv. Robot. **29**(5), 331–343 (2015)
5. Bourantas, G.C., Ghommem, M., Kagadis, G.C., Katsanos, K., Loukopoulos, V.C., Burganos, V.N., Nikiforidis, G.C.: Real-time tumor ablation simulation based on dynamic mode decomposition method. Med. Phys. **41**, 053301 (2014)
6. Box, G.E., Jenkins, G.M., Reinsel, G.C.: Time Series Analysis, 3rd edn. Prentice-Hall, Englewood Cliffs, NJ (1994)
7. Brunton, B.W., Johnson, L.A., Ojemann, J.G., Kutz, J.N.: Extracting spatial–temporal coherent patterns in large-scale neural recording using dynamic mode decomposition. J. Neurosci. Methods. **258**, 1–15 (2016). doi:10.1016/j.jneumeth.2015.10.010
8. Budišić, M., Mohr, R., Mezić, I.: Applied Koopmanism. Chaos **22**, 047510 (2012)
9. Chen, K., Tu, J., Rowley, C.: Variants of dynamic mode decomposition: boundary condition, Koopman, and Fourier analysis. J. Nonlinear Sci. **22**(6), 887–915 (2012)
10. Davison, E.J.: A method for simplifying linear dynamic systems. IEEE Trans. Autom. Control **11**(1), 93–101 (1966)
11. Dawson, S.T.M., Hemati, M.S., Williams, M.O., Rowley, C.W.: Characterizing and correcting for the effect of sensor noise in the dynamic mode decomposition. Exp. Fluids **57**(42), (2016)
12. Duke, D., Honnery, D., Soria, J.: Experimental investigation of nonlinear instabilities in annular liquid sheets. J. Fluid Mech. **691**, 594–604 (2012)
13. Duke, D., Soria, J., Honnery, D.: An error analysis of the dynamic mode decomposition. Exp. Fluids **52**(2), 529–542 (2012)
14. Fierro, R.D., Bunch, J.R.: Orthogonal projection and total least squares. Numer. Linear Algebra Appl. **2**(2), 135–153 (1995)
15. Fierro, R.D., Bunch, J.R.: Perturbation theory and orthogonal projection methods with applications to least squares and total least squares. Linear Algebra Its Appl. **234**, 71–96 (1996)
16. Fierro, R.D., Golub, G.H., Hansen, P.C., O'Leary, P.: Regularization by truncated total least squares. SIAM J. Sci. Comput. **18**(4), 1223–1241 (1997)
17. Gleser, L.J.: Estimation in a multivariate "error-in-variables" regression model: large sample results. Ann. Stat. **9**(1), 24–44 (1981)
18. Golub, G.H., Heath, M., Wahba, G.: Generalized cross-validation as a method for choosing a good ridge parameter. Technometrics **21**, 215–223 (1979)
19. Golub, G.H., Van Loan, C.F.: An analysis of the total least squares problem. SIAM J. Numer. Anal. **17**(6), 883–893 (1980)
20. Golub, G.H., Van Loan, C.F.: Matrix Computations, 3rd edn. Johns Hopkins University Press, Baltimore, MD (1996)
21. Goulart, P., Wynn, A., Pearson, D.: Optimal mode decomposition for high dimensional systems. In: 51st IEEE Conference on Descision and Control (2012)
22. Grosek, J., Kutz, J.N.: Dynamic mode decomposition for real-time background/foreground separation in video. ArXiv:1404.7592v1 (2014)
23. Guéniat, F., Mathelin, L., Pastur, L.R.: A dynamic mode decomposition approach for large and arbitrarily sampled systems. Phys. Fluids **27**, 025113 (2015)
24. Hansen, P.C.: Analysis of discrete ill-posed problems by means of the L-curve. SIAM Rev. **32**, 561–580 (1992)
25. Hasselmann, K.: PIPs and POPs: the reduction of complex dynamical systems using principal interaction and oscillation patterns. J. Geophys. Res. **93**(D9), 11015–11021 (1988)
26. Hemati, M.S., Williams, M.O., Rowley, C.W.: Dynamic mode decomposition for large and streaming datasets. Phys. Fluids **26**, 111701 (2014)
27. Ho, B.L., Kalman, R.E.: Effective construction of linear, state-variable models from input/output functions. Regelungstechnik **14**(12), 545–548 (1966)
28. Holmes, P., Lumley, J.L., Berkooz, G., Rowley, C.W.: Turbulence, Coherent Structures, Dynamical Systems and Symmetry, 2nd edn. Cambridge University Press, Cambridge (2012)
29. Jovanović, M.R., Schmid, P.J., Nichols, J.W.: Sparsity promoting dynamic mode decomposition. Phys. Fluids **26**, 024103 (2014)
30. Juang, J.N., Pappa, R.S.: An eigensystem realization algorithm for modal parameter-identification and model-reduction. J. Guid. Control Dyn. **8**(5), 620–627 (1985)
31. Koopman, B.O.: Hamiltonian systems and transformation in Hilbert space. Proc. Natl. Acad. Sci. **17**(5), 315–318 (1931)

32. Koopman, B.O., von Neumann, J.: Dynamical systems of continuous spectra. Proc. Natl. Acad. Sci. **18**(3), 255–263 (1932)
33. Kung, S.Y.: A new identification and model reduction algorithm via singular value decomposition. In: Proceedings of the 12th Asilomar Conference on Circuits, Systems, and Computers, pp. 705–714
34. Lanczos, C.: Applied Analysis. Dover Publications, New York (1988)
35. Markovsky, I., Van Huffel, S.: Overview of total least squares methods. Signal Process. **87**(10), 2283–2302 (2007)
36. Martinsson, P.G., Rokhlin, V., Tygert, M.: A randomized algorithm for the decomposition of matrices. Appl. Comput. Harmonic Anal. **30**(1), 47–68 (2011)
37. Mezić, I.: Spectral properties of dynamical systems, model reduction and decompositions. Nonlinear Dyn. **41**(1–3), 309–325 (2005)
38. Mezić, I.: Analysis of fluid flows via spectral properties of the Koopman operator. Ann. Rev. Fluid Mech. **45**, 357–378 (2013)
39. Morozov, V.A.: Methods for Solving Incorrectly Posed Problems. Springer, New York (1984)
40. Noack, B.R., Afanasiev, K., Morzynski, M., Tadmor, G., Thiele, F.: A hierarchy of low-dimensional models for the transient and post-transient cylinder wake. J. Fluid Mech. **497**, 335–363 (2003)
41. Proctor, J.L., Eckhoff, P.A.: Discovering dynamic patterns from infectious disease data using dynamic mode decomposition. Int. Health **7**(2), 139–145 (2015)
42. Rowley, C.W., Mezić, I., Bagheri, S., Schlatter, P., Henningson, D.: Spectral analysis of nonlinear flows. J. Fluid Mech. **641**, 115–127 (2009)
43. Schmid, P.: Dynamic mode decomposition of numerical and experimental data. J. Fluid Mech. **656**, 5–28 (2010)
44. Schmid, P.: Application of the dynamic mode decomposition to experimental data. Exp. Fluids **50**, 1123–1130 (2011)
45. Schmid, P., Li, L., Juniper, M., Pust, O.: Applications of the dynamic mode decomposition. Theor. Comput. Fluid Dyn. **25**, 249–259 (2011)
46. Schmid, P., Sesterhenn, J.: Dynamic mode decomposition of numerical and experimental data. In: 61st Annual Meeting of the APS Division of Fluid Dynamics (2008)
47. Semeraro, O., Bellani, G., Lundell, F.: Analysis of time-resolved PIV masurements of a confined turbulent jet using POD and Koopman modes. Exp. Fluids **53**, 1203–1220 (2012)
48. Sima, D.M., Van Huffel, S.: Level choice in truncated total least squares. Comput. Stat. Data Anal. **52**(2), 1103–1118 (2007)
49. Timmins, B.H., Wilson, B.W., Smith, B.L., Vlachos, P.P.: A method for automatic estimation of instantaneous local uncertainty in particle image velocimetry measurements. Exp. Fluids **53**(4), 1133–1147 (2012)
50. Tu, J.H., Rowley, C.W., Luchtenburg, D.M., Brunton, S.L., Kutz, J.N.: On dynamic mode decomposition: theory and applications. J. Comput. Dyn. **1**(2), 391–421 (2014)
51. Van Huffel, S., Vandewalle, J.: On the accuracy of total least squares and least squares techniques in the presence of errors on all data. Automatica **25**(5), 765–769 (1989)
52. Van Huffel, S., Vandewalle, J.: The total least squares problem: computational aspects and analysis. In: Frontiers in Applied Mathematics, vol. 9. SIAM, Philadelphia, PA (1991). doi:10.1137/1.9781611971002
53. von Neumann, J.: Proof of the quasi-ergodic hypothesis. Proc. Natl. Acad. Sci. **18**, 70–82 (1932)
54. Wieneke, B.: PIV uncertainty quantification from correlation statistics. Meas. Sci. Technol. **26**, 074002 (2015)
55. Williams, M.O., Kevrekidis, I.G., Rowley, C.W.: A data-driven approximation of the Koopman operator: extending dynamic mode decomposition. J. Nonlinear. Sci. **25**(6), 1307–1346 (2015)
56. Williams, M.O., Rowley, C.W., Kevrekidis, I.G.: A kernel-based method for data-driven Koopman spectral analysis. J. Comput. Dyn. **2**(2), 247–265 (2015)
57. Wilson, B.M., Smith, B.L.: Uncertainty on piv mean and fluctuating velocity due to bias and random errors. Meas. Sci. Technol. **24**(3), 035,302 (2013)
58. Wynn, A., Pearson, D., Ganapathisubramani, B., Goulart, P.: Optimal mode decomposition for unsteady flows. J. Fluid Mech. **733**, 473–503 (2013)
59. Zoltowski, M.D.: Generalized minimum norm and constrained total least squares with applications to array signal processing. Proc. SPIE **975**, 78–85 (1988)